Synthesis and Catalytic Properties of Sb2S3 Nanowire Bundles as Counter Electrodes for Dye-Sensitized Solar Cells

ARTICLE *in* THE JOURNAL OF PHYSICAL CHEMISTRY C · MAY 2013

Impact Factor: 4.77 · DOI: 10.1021/jp4016917

7 AUTHORS, INCLUDING:

Haijun Zhang

23 PUBLICATIONS **365** CITATIONS

SEE PROFILE

Letao Yang

Rutgers, The State University of New Jersey

7 PUBLICATIONS **186** CITATIONS

SEE PROFILE

Zhen Zhou

Nankai University

213 PUBLICATIONS **7,018** CITATIONS

SEE PROFILE

Wei Chen

Nankai University

21 PUBLICATIONS **653** CITATIONS

SEE PROFILE

THE JOURNAL OF PHYSICAL CHEMISTRY C

Article

pubs.acs.org/JPCC

Synthesis and Catalytic Properties of Sb_2S_3 Nanowire Bundles as Counter Electrodes for Dye-Sensitized Solar Cells

Haijun Zhang,[†,‡] Ming Ge,[§] Letao Yang,[†] Zhen Zhou,*[,†] Wei Chen,*[,†] Qingzhao Li,[§] and Lu Liu*[,†]

[†]Tianjin Key Laboratory of Environmental Remediation and Pollution Control, Key Laboratory of Advanced Energy Materials Chemistry (Ministry of Education), Institute of New Energy Material Chemistry, Nankai University, Tianjin 300071, China

[‡]School of Physics and Materials Science, Anhui University, Hefei 230039, China

[§]College of Chemical Engineering, School of Public Health, Hebei United University, Tangshan 063009, China

ABSTRACT: Through density functional theory (DFT) computations and experimental tests, we investigated the catalytic properties of Sb_2S_3 crystals with different facets used as counter electrodes (CEs) for dye-sensitized solar cells (DSSCs). The computations show that, compared with the (151) facet, the (211) facet has greater surface activity and better electrical conductivity but markedly lower band-edge levels, resulting in comparable catalytic activities for these two facets. To verify these predictions, we synthesized two Sb_2S_3 nanowire bundles, predominantly with exposed (151) and (211) facets, and found that DSSCs with these Sb_2S_3 CEs have similar $I-V$ curves and conversion efficiencies, which confirms the computations and suggests that the surface activity, electrical conductivity, specific surroundings, and band-edge positions should all be considered in the design of semiconductor CEs for DSSCs.

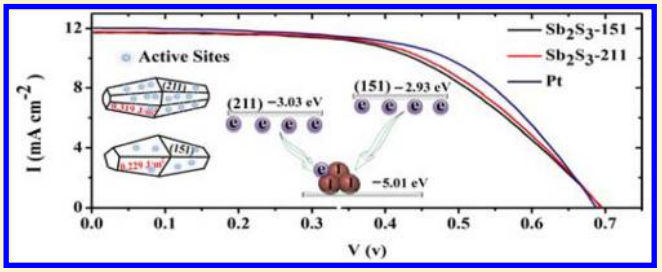

1. INTRODUCTION

Significant progress has been made in nanocrystal (NC) design during the past two decades. With the bottom-up approach, NCs can be made with uniform composition, size, and shape.[1−3] Because the physical and chemical properties of NCs are sensitive not only to the crystal size but also to the crystal shape and exposed facets, morphology-controlled synthesis of NCs has drawn increasing attention. Versatile inorganic materials, including metals[4,5] and semiconductors,[6−24] have been used in this effort, and many structurally unprecedented motifs have been discovered, such as polyhedrons, rods, belts, plates, and prisms.[25,26] Fine tuning of NCs was not previously achievable. Now, it is possible to explore whether there are new approaches for shape control that can lead catalysis research into new directions. For these reasons, recent studies have focused increasingly on shape-dependent catalytic behaviors of heterogeneous catalysts, including photo- and electrocatalysts.

It is well-known that catalytic processes occur on the surface of catalysts, and thus, the size, shape and exposed crystal facets of nanocrystals play a critical role in the activity and efficiency of catalysts.[27,28] Many reports have indicated that morphology- and facet-controlled NCs could be of great importance for the rational design and synthesis of useful catalysts, as well as for an understanding of catalytic phenomena. Most recently, Huang et al.[29] demonstrated that introducing amines as a surface controller allows the formation of concave Pt nanocrystals with (411) high-index facets through a facile wet-chemistry route. The as-prepared Pt nanocrystals were found to display a unique octapod morphology with (411) facets. The presence of exposed high-index (411) facets endows the concave Pt nanocrystals with excellent electrocatalytic activity in the oxidation of both formic acid and ethanol. Bi et al.[30] found that the (110) facets of Ag_3PO_4 exhibit a higher surface energy than the (100) planes and contribute significantly to the enhanced photocatalytic activity of Ag_3PO_4. These findings indicate that shape-controlled NCs can serve as novel model catalysts to bridge the gap between surface science and material science for heterogeneous catalysis because of exposed well-defined facets.

Morphology- and facet-controlled NCs are also prospective alternative catalysts for the counter electrodes (CEs) in dye-sensitized solar cells (DSSCs), as substitutes for the noble metal platinum with comparable electrocatalytic activities in reducing triiodide.[28] In this work, we investigated the structural and electronic properties, as well as the catalytic activities, of the (151) and (211) facets of Sb_2S_3 using periodic density functional theory (DFT) computations employing a slab model. Many DFT computations have focused on the structural and electronic properties of catalysts.[31−39] However, the specific surroundings, such as the pH value, electrolyte, and electronegativity, have not been taken into account in most cases. Based on the computations performed in this work, we synthesized Sb_2S_3 nanowire bundles with controlled morphologies and facets and found that the catalytic activity of Sb_2S_3

Received: February 18, 2013
Revised: April 20, 2013
Published: April 27, 2013

   dx.doi.org/10.1021/jp4016917 | J. Phys. Chem. C 2013, 117, 10285−10290

depends on not only the geometric and electronic structures but also the specific surroundings, namely, the electronegativity.

2. COMPUTATIONAL SECTION

Our periodic first-principles DFT computations were performed by employing a plane-wave basis set with the projector-augmented wave (PAW)[40,41] method to model the ion−electron interaction as implemented in the Vienna ab initio simulation package (VASP).[42] The generalized gradient approximation (GGA) with the PW91[43] functional and a 500 eV cutoff for the plane-wave basis set were employed in all computations. The tolerance for energy convergence was set at 10^{-4} eV, whereas the ionic relaxation was converged when the forces on the atoms were less than 10^{-3} eV/Å. The Brillouin zone was integrated using Monkhorst−Pack-generated sets of k points. We determined that $4 \times 4 \times 4$ k-point meshes and a $2 \times 2 \times 1$ supercell with 32 Sb and 48 S atoms were sufficient to reach convergence for bulk computations. On the basis of the equilibrium structures, the band structures of bulk Sb_2S_3 were computed along the special lines connecting the following high-symmetry points in k space: G (0, 0, 0), Z (0, 0, 0.5), T (0, 0.5, 0.5), Y (0, 0.5, 0), G (0, 0, 0), X (0.5, 0, 0), S (0.5, 0.5, 0), R (0.5, 0.5, 0.5), and U (0.5, 0, 0.5).

The surface computations were performed using the slab model, in which a finite number of crystal layers in a three-dimensional periodic-boundary-condition (PBC) cell was used to generate two surfaces through the introduction of a vacuum gap perpendicular to the surface. The structure of Sb_2S_3 belongs to the orthorhombic space group *Pbnm* (No. 62). In this work, the experimental values of the lattice parameters (a = 11.293 Å, b = 11.313 Å, c = 3.841 Å) were employed as the starting points. Both the atomic positions and lattice constants were optimized for bulk Sb_2S_3, whereas for the cleaved slab models, only the atomic positions were allowed to relax. In these computations, the (151) and (211) surfaces were considered, as shown in Figure 1. The vacuum gap must be large enough that

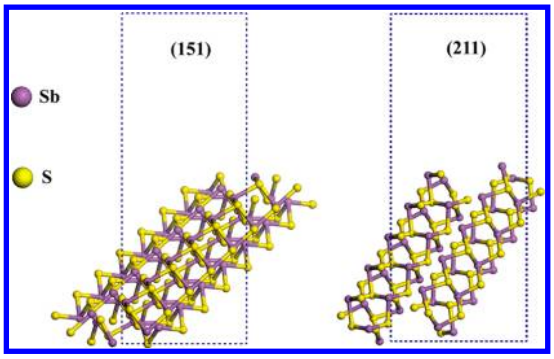

Figure 1. Slab models for (151) and (211) surfaces of Sb_2S_3. Blue dashed rectangles represent the periodic lattice frameworks.

the interactions between the periodic images perpendicular to the surface to be negligible. The slab must also have sufficient thickness that the structure in the middle of the slab is almost bulk-like. The surface energies computed in this work converged to 10^{-4} J/m^2 with respect to both the number of layers in the slab and the vacuum thickness, where a 17-Å vacuum gap was used throughout. Slabs with eight and six atomic layers models were used to simulate the (151) and (211) surfaces, respectively. A $3 \times 3 \times 1$ k-point grid was used for the surface relaxation, with the third vector perpendicular to the surface. Band structures of the fully relaxed slabs were computed along the special lines connecting the following high-symmetry points in k space: G (0, 0, 0), X (0.5, 0, 0), S (0.5, 0.5, 0) and Y (0, 0.5, 0).

3. EXPERIMENTAL SECTION

3.1. Material Preparation. All chemicals were of analytical grade and were used as received without further purification. Sb_2S_3 nanostructures were synthesized by a hydrothermal process. In a typical preparation, 0.3 g of $SbCl_3$, 0.4 g of thiocarbamide (or thiacetamide), and 0.4 g of poly(vinylpyrrolidone) (PVP) 40000 were added to 38 mL of absolute ethanol, and the suspension was stirred for 20 min, until a light yellowish precipitate formed. Afterward, the precipitate was transferred to a 50 mL Teflon-lined autoclave that was filled with water to 80% of its total volume. The autoclave was then heated at 150 °C for 24 h and allowed to cool to room temperature. The product in the autoclave was collected, washed with deionized water and absolute ethanol, and then dried and stored for further use.

3.2. Material Characterization. X-ray diffraction (XRD) was performed by using a model D/MAX2500 X-ray diffractometer (Rigaku) with Cu Kα radiation (λ = 1.54056 Å). The morphology was characterized by scanning electron microscopy (SEM, Hitachi-530, SEM/EDX JEOL JSM-6700F), transmission electron microscopy (TEM, JEOL-2010, operating voltage of 200 kV), and high-resolution TEM (HRTEM, FEI Tecnai G^{2}F-20). The elemental composition was analyzed by X-ray photoelectron spectroscopy (XPS, Kratos Axis Ultra DLD).

3.3. Photovoltaic Tests. Approximately 0.05 g of Sb_2S_3 powder was mixed with 0.5 mL of 2.5% polyethylene glycol (PEG) 20000 solution and stirred until a fluid mixture formed. A film was then made using the doctor-blade method on a fluorine-doped tin oxide (FTO) conductive glass (LOF, TEC-15, 15 W/square). The film was heated at 450 °C for 1 h under the protection of argon to obtain the Sb_2S_3 counter electrode. A commercial TiO_2 sol (Solaronix, Ti-Nanoxide T/SP) was used to prepare the TiO_2 film on the FTO glass using the doctor-blade method, and the film was soaked in an N-719 dye solution (in ethanol) for 24 h to obtain the dye-sensitized TiO_2 electrode. Dye-sensitized solar cells were assembled by injecting the electrolyte into the aperture between the dye-sensitized TiO_2 electrode and the counter electrode. The liquid electrolyte was composed of 0.05 M I_2, 0.1 M LiI, 0.6 M 1,2-dimethyl-3-propylimidazolium iodide (DMPII), and 0.5 M 4-*tert*-butyl pyridine with acetonitrile as the solvent. Surlyn 1702 was used as the spacer between the two electrodes. The two electrodes were clipped together, and solid paraffin was used as the sealant to prevent the electrolyte solution from leaking. The effective cell area was 0.25 cm^2. Photocurrent−voltage (I−V) curves were measured with a Zahner IM6ex electrochemical workstation using a Trusttech CHF-XM-500W source under simulated sun illumination (Global AM 1.5, 100 mW cm^{-2}).

4. RESULTS AND DISCUSSION

After full relaxation of atomic positions and lattice constants, we obtained a crystal lattice with parameter values of a = 11.200 Å, b = 3.875 Å, and c = 12.024 Å, which are slightly larger than the experimental values (a = 11.282 Å, b = 3.830 Å, c = 11.225 Å).[44] Within the fully relaxed slab models, there was a slight inward and outward motion of the surface Sb and S atoms, due

dx.doi.org/10.1021/jp4016917 | J. Phys. Chem. C 2013, 117, 10285−10290

to surface reconstruction. The slightly larger lattice constants of Sb_2S_3 might result from the common overestimate for these crystals within the DFT framework.[45,46]

Surface energy is one of the key factors controlling the number of active sites and, accordingly, the catalytic activity of Sb_2S_3 catalysts. Therefore, we first calculated the surface energies of Sb_2S_3 crystals with exposed (151) and (211) facets. The standard method for calculating the surface energy, E_{surf}, is based on the general expression[29,47,48]

$$E_{surf} = \lim_{n\to\infty} \frac{E^n_{slab} - nE_{bulk}}{2A} \quad (1)$$

where E^n_{slab} is the total energy of the slab, E_{bulk} is the total energy per unit cell of the bulk, n is the number of bulk unit cells contained in the slab, and A is the surface area of each side of the slab. When the number of bulk unit cells n becomes sufficiently large and convergence is approached, E_{surf} can be calculated as

$$E_{surf} = \frac{E^n_{slab} - nE_{bulk}}{2A} \quad (2)$$

The calculated surface energies of the (151) and (211) facets are listed in Table 1. As a result of the different surface

Table 1. Surface Energies and Band Gaps Calculated for (151) and (211) Facets of Sb_2S_3

facet	surface energy (J/m^2)	band gap (eV)
(151)	0.229	1.36
(211)	0.319	1.30

reconstructions and configurations, the (211) facet was found to have a higher surface energy than the (151) facet, indicating that Sb_2S_3 with exposed (211) facets has more active sites than Sb_2S_3 with exposed (151) facets. Considering the surface configuration and activity, one can strongly recommend the (211) facets of Sb_2S_3 as a CE for DSSCs, whereas the (151) facets of Sb_2S_3 are ill-suited for this purpose.

Because the electrical conductivity of a CE, which is affected by the carrier concentration, should determine its efficiency of electron transfer (to I_3^- in the electrolyte), the electrical conductivity is another critical factor that influences the catalytic activity of CEs in DSSCs. To analyze the electronic properties, the band structures for bulk and slab-model Sb_2S_3 were computed, and the results are shown in Figure 2. It can be seen from Figure 2a that bulk Sb_2S_3 has an indirect band gap of 1.40 eV with a valence-band maximum (VBM) at the G point and a conduction-band minimum (CBM) at a general point along GX. To better understand the electronic structures near the gap region, we computed the densities of states of bulk and faceted Sb_2S_3 and found that the bottom of the conduction band is mainly composed of Sb 5p states whereas the top of the valence band is composed of Sb 5s and S 3p orbitals.

It is well-known that the CBM of intrinsic semiconductors is unoccupied at 0 K. Only if the surrounding temperature rises above 0 K can electrons be thermodynamically excited from the valence band to the conduction band and holes be left in the valence band. Furthermore, the carrier concentration, one dominant factor controlling the electrical conductivity of a semiconductor, is inversely proportional to the band gap and directly proportional to the temperature. At strictly equivalent thermodynamic conditions, a semiconductor with a smaller band gap should have better electrical conductivity. We

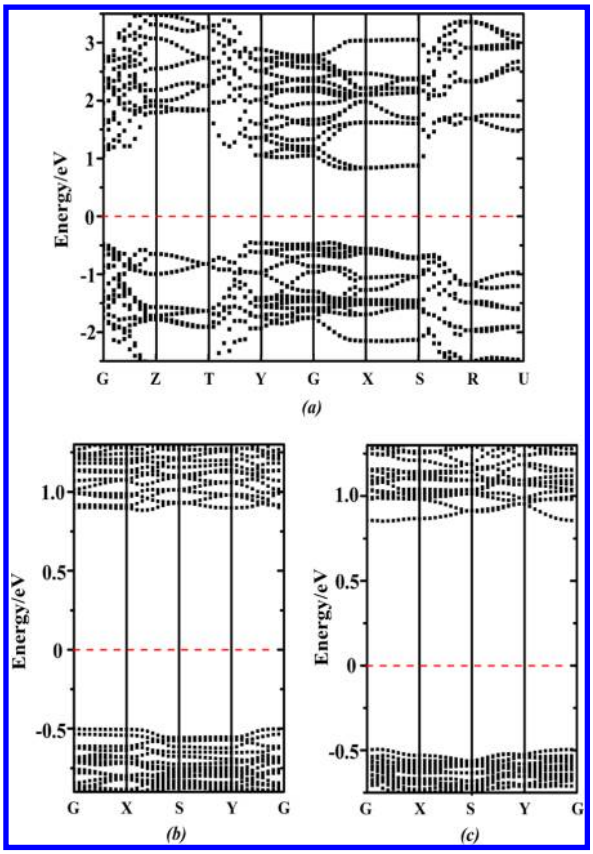

Figure 2. Band structures of Sb_2S_3: (a) supercell, (b) (151) facet, and (c) (211) facet.

compared the band gaps of the facets of the Sb_2S_3 crystal, as listed at Table 1, and found the (151) facet of Sb_2S_3 to have a slightly larger band gap. As the result, under thermodynamic excitation, the carrier concentration of the (211) facet is slightly higher than that of the (151) facet, and thus, the electrical conductivity of the (211) facet is better to a small degree.

With respect to the surface activity and electrical conductivity, the (211) facet of Sb_2S_3 should have better catalytic activity for reducing the redox couple. However, there is another factor that determines the catalytic activity of CE. As for other catalysts, the efficiency of electron transfer is affected by the positions of the receiving molecule's lowest unoccupied molecule orbital (LUMO) and the catalyst's CBM.[49] Generally, an electron located in a higher energy level can more facilely transfer to a lower energy level. Accordingly, we calculated the CBMs of neutral (151) and (211) facets of Sb_2S_3 and obtained energy levels of −3.84 and −3.79 eV, respectively, implying comparable electron-transfer rates for these two faceted Sb_2S_3 crystals. Nevertheless, during the catalytic reduction process, the surface of the CE is negative and filled with electrons. Therefore, to evaluate energy levels under these conditions, we added two electrons to each slab. The energy levels of the LUMO of I_3^- and the CBMs of the negatively charged Sb_2S_3 facets are presented in Figure 3. The LUMO of I_3^- is much lower than the CBMs of the Sb_2S_3 facets, indicating that electrons can easily transfer from the Sb_2S_3 facets to I_3^-.[50] Furthermore, the position of CBM for the (151) facet is above that for the (211) facet, meaning that electron transfer from the former is more effective.

To verify the results of the computations, we synthesized Sb_2S_3 nanowire bundles and characterized the catalytic

dx.doi.org/10.1021/jp4016917 | J. Phys. Chem. C 2013, 117, 10285−10290

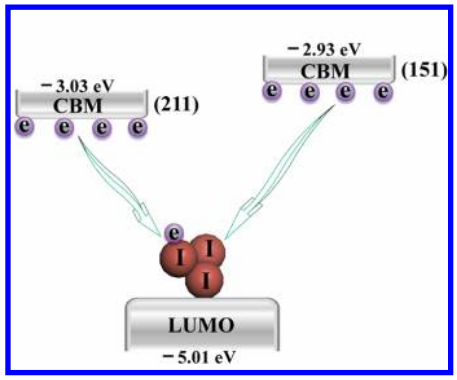

Figure 3. Schematic diagram of electron transfer from the Sb_2S_3 surface to I_3^-.

performances of the as-prepared samples. As shown in the XRD patterns (Figure 4a,b), the samples denoted Sb_2S_3-151 and

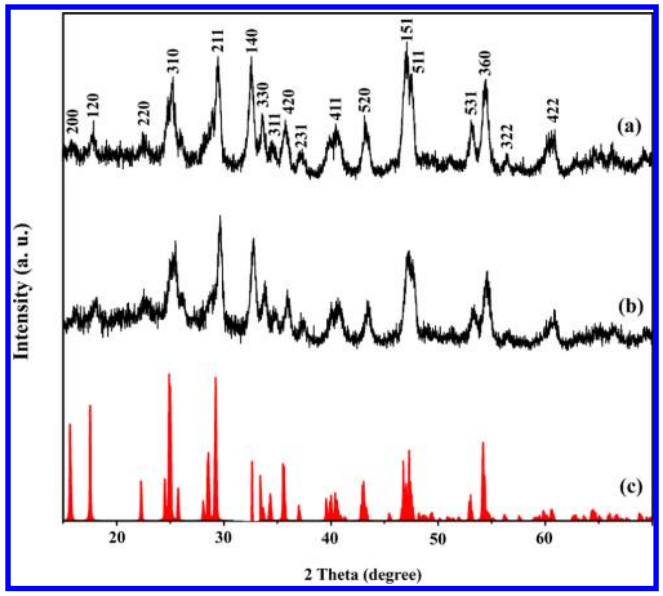

Figure 4. XRD patterns of as-synthesized (a) Sb_2S_3-151 and (b) Sb_2S_3-211 samples. (c) Standard XRD patterns of orthorhombic Sb_2S_3 (JCPDS no. 42-1393).

Sb_2S_3-211 had the strongest (151) and (211) peaks, respectively, indicating that the corresponding preferred orientations were along the (151) and (211) planes. This is further illustrated in Figure 5.

It can be seen from typical SEM images (Figure 5a,b) that the Sb_2S_3 samples were constructed of nanowire-bundle nanostructures. As shown in Figure 5c–f, the fringe spacings of 0.201 and 0.255 nm agree well with the values for the $(20\bar{2})$ and $(1\bar{2}0)$ lattice planes (0.204 and 0.259 nm), respectively, of orthorhombic Sb_2S_3. Accordingly, the Sb_2S_3 samples had dominantly exposed (151) and (211) surfaces, which are perpendicular to the $(20\bar{2})$ and $(1\bar{2}0)$ planes, respectively.

To further verify the computations, we investigated the electrical conductivity of the Sb_2S_3 nanostructures by characterizing the impedance, and the results are shown in Figure 6a. Compared with Sb_2S_3-151, Sb_2S_3-211 was found to have a slightly lower impedance and, thus, better electrical conductivity; this is in agreement with the computational predictions obtained in this work. The $I-V$ curves of two DSSCs with TiO_2 film as the photoelectrode and Sb_2S_3-151 or

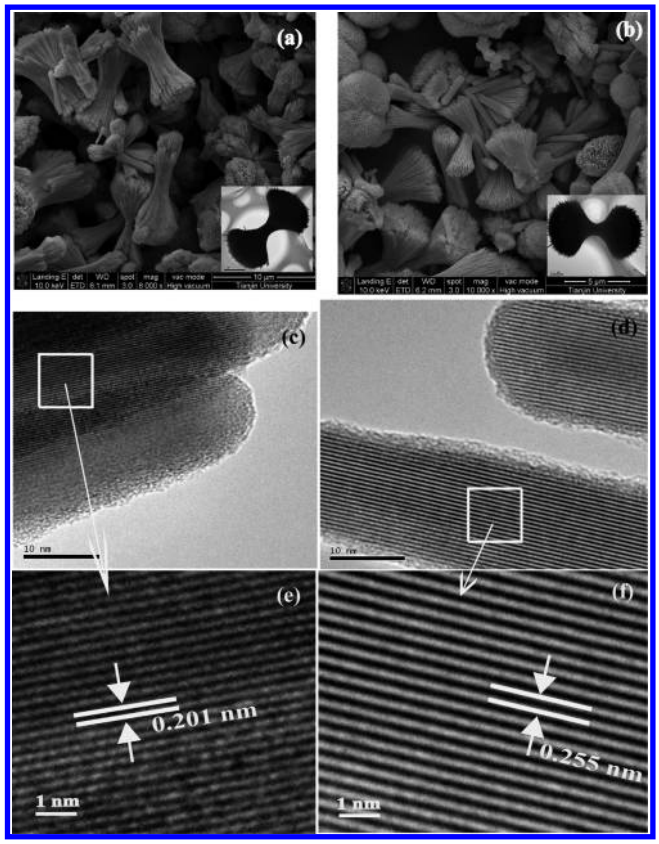

Figure 5. (a,b) SEM, TEM (insets in panels a and b), and (c–f) HRTEM images of (a,c,e) Sb_2S_3-151 and (b,d,f) Sb_2S_3-211.

Sb_2S_3-211 as the CE were also compared. Notably, the Sb_2S_3-151 and Sb_2S_3-211 CEs were found to give similar $I-V$ curves, as shown in Figure 6b.

We offer the following explanations for the aforementioned findings. The (211) facet of Sb_2S_3 has a higher surface energy and better electrical conductivity than the (151) facet. However, the relative CBM position of negatively charged (211) facets of Sb_2S_3 is below that of negatively charged (151) facets (Figure 3), giving the (211) facet of Sb_2S_3 a lower electron-transfer efficiency. Consequently, the (211) and (151) facets of Sb_2S_3 have comparable catalytic activities, and the overall $I-V$ properties of the Sb_2S_3-211 and Sb_2S_3-151 CEs are similar. Furthermore, DSSCs with Sb_2S_3-151 and Sb_2S_3-211 CEs annealed at 450 °C showed close conversion efficiencies of 4.39% and 4.52%, respectively, under the same conditions. Additionally, these conversion efficiencies suggest the possibility of using Sb_2S_3 nanocrystals, with exposed active facets, as high-efficiency Pt-free CEs. The geometric and electronic design of semiconductor nanocrystals appears to be an important approach for enhancing the conversion efficiency of DSSCs.

5. CONCLUSIONS

In summary, our DFT computations show that the (211) facet of Sb_2S_3 has a higher surface energy and slightly smaller band gap, but a lower CB level, than the (151) facet, indicating that Sb_2S_3 with exposed (211) facets should have more surface active sites and better electrical conductivity but a lower electron-transfer rate. As a result, these two faceted Sb_2S_3 CEs have similar catalytic activities. To validate these predictions, we synthesized Sb_2S_3 nanowire bundles with dominantly exposed

dx.doi.org/10.1021/jp4016917 | J. Phys. Chem. C 2013, 117, 10285−10290

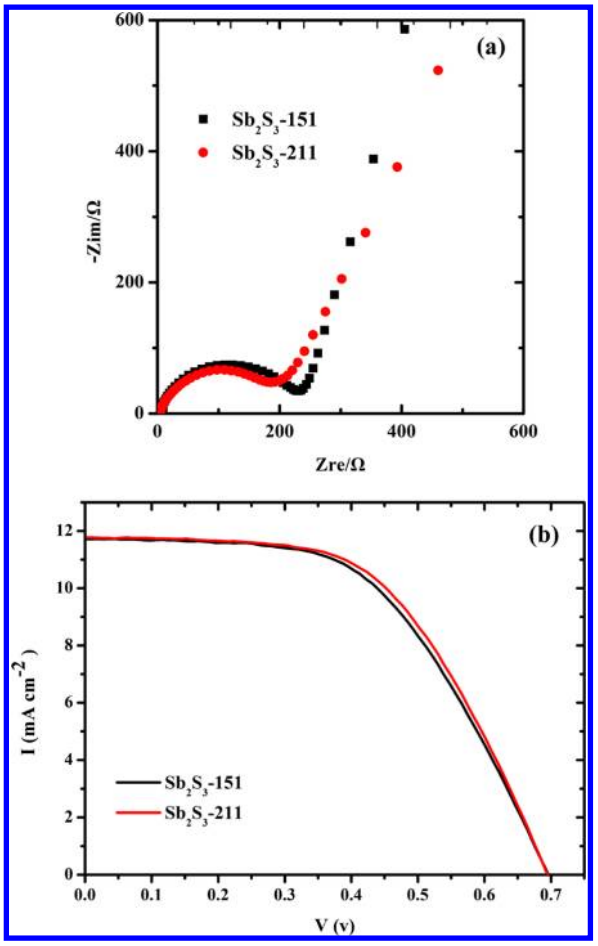

Figure 6. (a) Impedance spectra and (b) *I*−*V* curves of Sb_2S_3-151 and Sb_2S_3-211 samples.

(151) and (211) facets and measured their impedance properties, *I*−*V* curves, and conversion efficiencies. Compared with Sb_2S_3 with dominantly exposed (151) facets, Sb_2S_3 with dominantly exposed (211) facets has a slightly better electrical conductivity but similar *I*−*V* characteristics and conversion efficiency, in accordance with the computations. Therefore, the surface activity, electrical conductivity, specific surroundings, and band-edge positions should all be considered in the design of semiconductor CEs for DSSCs. These findings are of value for better understanding the catalytic properties of semiconductor CEs and providing some guidance for the design of Pt-free counter electrodes.

AUTHOR INFORMATION

Corresponding Author

*E-mail: zhouzhen@nankai.edu.cn (Z.Z.), chenwei@nankai.edu.cn (W.C.), liul@nankai.edu.cn (L.L.).

Notes

The authors declare no competing financial interest.

ACKNOWLEDGMENTS

This work was supported by the Ministry of Science and Technology (Grant 2011DFB50300), Tianjin Municipal Science and Technology Commission (Grants 11JCZDJC24800 and 12JCZDJC28100), China-U.S. Center for Environmental Remediation and Sustainable Development, Anhui Provincial Education Department for Scientific Research of College and Universities (KJ2013A018), and Youth Foundation of Anhui University in China.

REFERENCES

(1) Mehta, R. J.; Zhang, Y. L.; Karthik, C.; Singh, B.; Siegel, R. W.; Borca-Tasciuc, T.; Ramanath, G. *Nat. Mater.* **2012**, *11*, 233−240.
(2) Tian, B. Z.; Xie, P.; Kempa, T. J.; Bell, D. C.; Lieber, C. M. *Nat. Nanotechnol.* **2009**, *4*, 824−829.
(3) Liu, L. P.; Zhuang, Z. B.; Xie, T.; Wang, Y. G.; Li, J.; Peng, Q.; Li, Y. D. *J. Am. Chem. Soc.* **2009**, *131*, 16423−16429.
(4) Lim, B.; Jiang, M. J.; Tao, J.; Camargo, P. H. C.; Zhu, Y. M.; Xia, Y. N. *Adv. Funct. Mater.* **2009**, *19*, 189−200.
(5) Xia, Y.; Xiong, Y. J.; Lim, B.; Skrabalak, S. E. *Angew. Chem., Int. Ed.* **2009**, *48*, 60−103.
(6) Niederberger, M. *Acc. Chem. Res.* **2007**, *40*, 793−800.
(7) Zheng, Q.; Kang, H.; Yun, J.; Lee, J.; Park, J. H.; Baik, S. *ACS Nano* **2011**, *5*, 5088−5093.
(8) Li, H. Q.; Qu, J.; Cui, Q. Z.; Xu, H. B.; Luo, H. M.; Chi, M. F.; Meisner, R. A.; Wang, W.; Dai, S. *J. Mater. Chem.* **2011**, *21*, 9487−9490.
(9) Zhou, Y.; Antonietti, M. *J. Am. Chem. Soc.* **2003**, *125*, 14960−14961.
(10) Yang, H. G.; Zeng, H. C. *J. Phys. Chem. B* **2004**, *108*, 3492−3495.
(11) Yang, H. G.; Zeng, H. C. *Angew. Chem., Int. Ed.* **2004**, *43*, 5206−5209.
(12) Liu, B.; Zeng, H. C. *J. Am. Chem. Soc.* **2004**, *126*, 8124−8125.
(13) Chang, Y.; Teo, J. J.; Zeng, H. C. *Langmuir* **2005**, *21*, 1074−1079.
(14) Liu, B.; Zeng, H. C. *J. Am. Chem. Soc.* **2004**, *126*, 16744−16746.
(15) Mo, M.; Yu, J. C.; Zhang, L.; Li, S.-K. A. *Adv. Mater.* **2005**, *17*, 756−760.
(16) Sargent, E. H. *Nat. Photonics* **2012**, *6*, 133−135.
(17) Fan, X.; Zhang, M. L.; Shafiq, I.; Zhang, W. J.; Lee, C. -S.; Lee, S. -T. *Adv. Mater.* **2009**, *21*, 2393−2396.
(18) Jun, Y. W.; Choi, J. S.; Cheon, J. *Angew. Chem., Int. Ed.* **2006**, *45*, 3414−3439.
(19) Kale, B. B.; Baeg, J. -O.; Lee, S. M.; Chang, H.; Moon, S. -J.; Lee, C. W. *Adv. Funct. Mater.* **2006**, *16*, 1349−1354.
(20) Fang, X. S.; Wu, L. M.; Hu, L. F. *Adv. Mater.* **2011**, *23*, 585−598.
(21) Zhao, L. J.; Hu, L. F.; Fang, X. S. *Adv. Funct. Mater.* **2012**, *22*, 1551−1566.
(22) Fang, X. S.; Hu, L. F.; Huo, K. F.; Gao, B.; Zhao, L. J.; Liao, M. Y.; Chu, P. K.; Bando, Y.; Golberg, D. *Adv. Funct. Mater.* **2011**, *21*, 3907−3915.
(23) Heo, J. H.; Im, S. H.; Kim, H. -J.; Boix, P. P.; Lee, S. J.; Seok, S. I.; Mora-Seró, I.; Bisquert, J. *J. Phys. Chem. C* **2012**, *116*, 20717−20721.
(24) Itzhaik, Y.; Niitsoo, O.; Page, M.; Hodes, G. *J. Phys. Chem. C* **2009**, *113*, 4254−4256.
(25) Wang, X.; Zhuang, J.; Peng, Q.; Li, Y. D. *Nature* **2005**, *437*, 121−124.
(26) Liang, X.; Wang, X.; Zhuang, J.; Chen, Y. T.; Wang, D. S.; Li, Y. D. *Adv. Funct. Mater.* **2006**, *16*, 1805−1813.
(27) Zhou, K. B.; Li, Y. D. *Angew. Chem., Int. Ed.* **2012**, *51*, 602−613.
(28) Zhang, H. J.; Yang, L. T.; Liu, Z.; Ge, M.; Zhou, Z.; Chen, W.; Li, Q. Z.; Liu, L. *J. Mater. Chem.* **2012**, *22*, 18572−18577.
(29) Huang, X. Q.; Zhao, Z. P.; Fan, J. M.; Tan, Y. M.; Zheng, N. F. *J. Am. Chem. Soc.* **2011**, *133*, 4718−4721.
(30) Bi, Y. P.; Ouyang, S. X.; Umezawa, N.; Cao, J. Y.; Ye, J. H. *J. Am. Chem. Soc.* **2011**, *133*, 6490−6492.
(31) Liu, Z. P.; Hu, P. *J. Am. Chem. Soc.* **2002**, *124*, 14770−14779.
(32) Liu, Z. P.; Jenkins, S. J.; King, D. *J. Am. Chem. Soc.* **2003**, *125*, 14660−14661.
(33) Liu, Z. P.; Jenkins, S. J.; King, D. A. *J. Am. Chem. Soc.* **2004**, *126*, 10746−10756.
(34) Yang, K. S.; Dai, Y.; Huang, B. B.; Whangbo, M. H. *Chem. Mater.* **2008**, *20*, 6528−6534.

(35) Sun, H. G.; Fan, W. L.; Li, Y. L.; Cheng, X. F.; Li, P.; Hao, J. C.; Zhao, X. *Phys. Chem. Chem. Phys.* **2011**, *13*, 1379−1385.
(36) Oshikiri, M.; Boero, M. *J. Phys. Chem. B* **2006**, *110*, 9188−9194.
(37) Huang, W. L. *J. Comput. Chem.* **2009**, *30*, 1882−1891.
(38) Zhang, H. J.; Liu, L.; Zhou, Z. *Phys. Chem. Chem. Phys.* **2012**, *14*, 1286−1292.
(39) Zhang, H. J.; Liu, L.; Zhou, Z. *RSC Adv.* **2012**, *2*, 9224−9229.
(40) Blöchl, P. E. *Phys. Rev. B* **1994**, *50*, 17953−17979.
(41) Kresse, G.; Joubert, D. *Phys. Rev. B* **1999**, *59*, 1758−1775.
(42) Kresse, G.; Hafner, J. *Phys. Rev. B* **1994**, *49*, 14251−14265.
(43) Perdew, J. P.; Wang, Y. *Phys. Rev. B* **1992**, *45*, 13244−13249.
(44) Kyono, A.; Kimata, M. *Am. Mineral.* **2004**, *89*, 932−940.
(45) Caracas, R.; Gonze, X. *Phys. Chem. Miner.* **2005**, *32*, 295.
(46) Ben Nasr, T.; Maghraoui-Meherzi, H.; Ben Abdallah, H.; Bennaceur, R. *Physica B* **2011**, *406*, 287−292.
(47) Beltrán, A.; Andrés, J.; Sambrano, J. R.; Longo, E. *J. Phys. Chem. A* **2008**, *112*, 8943−8952.
(48) Labat, F.; Baranek, P.; Adamo, C. *J. Chem. Theory Comput.* **2008**, *4*, 341−352.
(49) Martsinovich, N.; Troisi, A. *Energy Environ. Sci.* **2011**, *4*, 4473−4495.
(50) De Angelis, F.; Fantacci, S.; Selloni, A.; Grätzel, M.; Nazeeruddin, M. K. *Nano Lett.* **2007**, *7*, 3189−3195.